


Linear stability of real-fluid mixing layers at supercritical pressures

Cite as: Phys. Fluids **34**, 084106 (2022); <https://doi.org/10.1063/5.0101342>

Submitted: 31 May 2022 • Accepted: 14 July 2022 • Accepted Manuscript Online: 16 July 2022 • Published Online: 09 August 2022

 Xingjian Wang (王兴建), Tao Liu (柳涛), Dongjun Ma (马东军), et al.

COLLECTIONS

Paper published as part of the special topic on [Centennial of the Kármán-Pohlhausen Momentum-Integral Approach](#)



[View Online](#)



[Export Citation](#)



[CrossMark](#)

ARTICLES YOU MAY BE INTERESTED IN

[Trajectory-optimized cluster-based network model for the sphere wake](#)

Phys. Fluids **34**, 085110 (2022); <https://doi.org/10.1063/5.0098655>

[General framework for the study of dynamical properties and arrested states of ionic liquids](#)

Phys. Fluids **34**, 084108 (2022); <https://doi.org/10.1063/5.0095000>

[Effect of rough wall on drag, lift, and torque on an ellipsoidal particle in a linear shear flow](#)

Phys. Fluids **34**, 083312 (2022); <https://doi.org/10.1063/5.0093232>

APL Machine Learning

Open, quality research for the networking communities

Now Open for Submissions

[LEARN MORE](#)



Linear stability of real-fluid mixing layers at supercritical pressures

Cite as: Phys. Fluids **34**, 084106 (2022); doi: [10.1063/5.0101342](https://doi.org/10.1063/5.0101342)

Submitted: 31 May 2022 · Accepted: 14 July 2022 ·

Published Online: 9 August 2022





View Online



Export Citation



CrossMark

Xingjian Wang (王兴建),^{1,a)}  Tao Liu (柳涛),² Dongjun Ma (马东军),² and Vigor Yang (杨威迦)^{3,a)} 

AFFILIATIONS

¹Department of Power and Energy Engineering, Tsinghua University, Beijing 100084, China

²Department of Mechanical and Nuclear Engineering, The Pennsylvania State University, University Park, Pennsylvania 16802, USA

³School of Aerospace Engineering, Georgia Institute of Technology, Atlanta, Georgia 30332, USA

Note: This paper is part of the special topic, Centennial of the Kármán-Pohlhausen Momentum-Integral Approach.

^{a)}Authors to whom correspondence should be addressed: xingjianwang@tsinghua.edu.cn and vigor.yang@aerospace.gatech.edu

ABSTRACT

Linear stability analysis is a useful tool for the exploration of the initial evolution of flow motions in mixing layers. A real fluid mixing layer exhibits strong property variations and, thus, may present stability behaviors distinct from its ideal gas counterpart. The present study carries out spatial and temporal stability analyses of nitrogen mixing layers at supercritical conditions, with special attention to the density stratification induced by the temperature and velocity gradients across the mixing layer. The differences between the ideal gas and real fluid approaches are discussed. The maximum spatial growth rate and the most unstable frequency evaluated based on the real fluid density profile are found to be substantially lower than their ideal gas counterparts near the critical point, where an inflection of the density distribution occurs in the mixing layer. Across the inflection point, the strong density stratification arising from the real fluid effect tends to stabilize the mixing layer. The maximum growth rate and the most unstable frequency do not show a monotonic trend with the ratios of temperature and density. In the absence of the inflection point, however, the mixing layer is destabilized and features a substantially higher maximum spatial growth rate at lower ratios of density and temperature. The most unstable frequency and the maximum spatial growth rate increase with increasing pressure. The real fluid effect diminishes when the pressure is away from the critical value or when there is no inflection point in the density profile. The temporal stability analysis also indicates that a detailed density distribution plays a key role in dictating the stability characteristics of mixing layers at supercritical pressures.

Published under an exclusive license by AIP Publishing. <https://doi.org/10.1063/5.0101342>

I. INTRODUCTION

The mixing layer is a principal feature of many complex shear flows and has been extensively studied in a wide variety of applications.^{1–9} Linear stability analyses are commonly used to characterize the initial-stage development of a mixing layer before the establishment of full-scale vortical motions in the downstream region, which subsequently determine the overall flow behaviors.¹⁰ Huerre and Monkewitz¹¹ conducted a review of early works on the absolute/convective and local/global stability characteristics of mixing layers. The propagation of a linear instability wave satisfies a dispersion relation that can be solved either theoretically or numerically. Extensive efforts have revolved around linear stability analyses of ideal gas mixing layers, with emphasis on the effects of various flow parameters, including density and velocity ratios, fluid compressibility, and species combination, among others.^{12–20}

Yu and Monkewitz¹³ explored the effect of variable density on absolute and convective instabilities of two-dimensional jets and

wakes. It was found that the low density of the high-speed stream promotes absolute instability while the low density of the low-speed stream has the opposite effect. Shin and Ferziger¹⁵ studied the effects of mean flow profiles, heat release, and variable transport properties on the linear stability of reacting mixing layers. The flow profiles retrieved from the solutions of boundary-layer equations along with variable transport properties were found to be a more realistic representation of an actual flow than analytically prescribed functions. Kozusko *et al.*¹⁶ performed spatial stability of a compressible binary mixing layer. The ratio of molecular weight between the slow and fast streams played a significant role in determining the stability characteristics. Day *et al.*¹⁷ numerically investigated the combined effects of compressibility, heat release, and ratios of density and velocity on the spatial stability characteristics of a compressible reacting mixing layer. They concluded that the outer modes associated with fast and slow freestreams tend to impose a lower global reaction rate than the central

mode associated with the Kelvin–Helmholtz instability. Regime diagrams were developed to illustrate the dominant instability mode under various parametric sets. Kennedy and Chen¹⁸ found that the jet-to-ambient temperature ratio poses a greater impact on the instability growth rate than fluid compressibility for high Reynolds number flows. Fedioun and Lardjane¹⁹ proposed an empirical model to predict the stability features of compressible flows using incompressible results. All of the aforementioned studies were devoted to ideal gas mixing layers and did not take into account real fluid effects.

Real fluids are, however, commonly encountered in natural sciences and engineering applications when the pressure exceeds the thermodynamic critical value of the fluid of concern.^{21–23} A representative example is liquid-fueled combustion devices. Liquid fuel is often delivered at a subcritical temperature into a chamber operating at a supercritical pressure. The injected fuel then heats up and experiences a thermodynamic phase transition into the supercritical regime.²¹ Rapid variations of thermophysical properties occur and lead to strong density stratification. Such phenomena must be taken into account in stability analyses of real fluid mixing layers.^{24,25} Along each isobaric line in the density distribution, there exists an inflection point, across which a steep gradient of density with respect to temperature appears. Zong *et al.*²⁴ found that the strong density stratification across the inflection point has a stabilizing effect on flow development. Okong'o and Bellan²⁶ investigated real fluid effects on the mean flow and the temporal stability of inviscid binary mixing layers at supercritical pressure. They found that the similarity profile of the mean flow caused by the real fluid effect showed deviation from the incompressible error function solution. It leads to a larger temporal growth rate and shortens the most unstable wavelength compared to the error function solution.

Yecko *et al.*²⁷ investigated the viscous modes in the temporal stability of two-phase mixing layers by adopting a composite error function profile in each phase. An interfacial mode and two Tollmien–Schlichting type modes were found to be related to the presence of the viscous boundary layer. For water atomization in air, the viscous stability analysis resulted in better agreement with experimental measurements than its inviscid counterpart.²⁸ Govindarajan and Sahu²⁹ reviewed the alterations of flow stability by viscosity stratification in model shear flows and various industrial applications. Roy and Segal³⁰ performed a spatial stability analysis of viscous jets to explore jet breakup mechanisms in both subcritical and supercritical environments. A dispersion relation was derived to quantify the effects of surface tension and Weber number on the peak growth rate. As the fluid transits from the subcritical to the supercritical state, surface tension diminishes and the Weber number increases. The peak growth rate approaches an asymptote with a high Weber number at supercritical pressure. Fu and Yang³¹ conducted a temporal stability analysis of a transcritical shear layer and examined the effects of density stratification and ratios of density, velocity, and temperature. Fu *et al.*³² extended the analysis to study the binary mixing layer at supercritical pressure. A linear gradient theory was employed to obtain the density profile at the interface. The maximum temporal growth rate was found to increase with increasing pressure or decreasing temperature.

In the present work, the spatial and temporal stability behaviors of supercritical mixing layers with density stratification are investigated over a wide range of pressure in order to shed light on real fluid effects in the initial stage of flow evolution. A variety of density

distributions are considered, along with different pressures and ratios of velocity and temperature. Results are compared with their ideal gas counterparts. The paper is organized as follows. Section II presents the theoretical formulation of the disturbance equations for real fluid mixing layers and introduces the distributions of mean flow properties. The results of the stability analyses are discussed in Sec. III, and conclusions are presented in Sec. IV.

II. THEORETICAL FORMULATION

For real fluid mixing layers of concern, the Reynolds numbers are typically greater than $O(10^2)$. The viscous effect on the fluctuating flowfield can, thus, be ignored.²⁶ If heat conduction and body force are insignificant, the conservation equations of mass, momentum, and energy can be written in the following primitive form:

$$\frac{\partial \rho}{\partial t} + \rho \frac{\partial u_j}{\partial x_j} + u_j \frac{\partial \rho}{\partial x_j} = 0, \tag{1}$$

$$\frac{\partial u_i}{\partial t} + u_j \frac{\partial u_i}{\partial x_j} + \frac{1}{\rho} \frac{\partial p}{\partial x_i} = 0, \tag{2}$$

$$\rho C_p \left(\frac{\partial T}{\partial t} + u_j \frac{\partial T}{\partial x_j} \right) = \beta T \left(\frac{\partial p}{\partial t} + u_j \frac{\partial p}{\partial x_j} \right), \tag{3}$$

where ρ is the density, u_i is the velocity component in the i -direction, p is the pressure, T is the temperature, C_p is the constant-pressure specific heat, and β is the volume thermal expansion coefficient. A real fluid equation of state (EOS) is required to model the thermodynamic relationship. The present study employs a modified Soave–Redlich–Kwong (SRK) EOS,³³

$$p = \frac{RT}{V - b} - \frac{a\alpha}{V(V + b)}, \tag{4}$$

where V is the molar volume and R is the universal gas constant. The model coefficients $a\alpha$ and b account for attractive and repulsive forces between molecules, respectively. Equation (4) can also be written in a cubic form in terms of the compressibility factor Z ,

$$Z^3 - Z^2 + Z(A - B - B^2) - AB = 0, \tag{5}$$

where $A = a\alpha p/R^2 T^2$ and $B = bp/RT$.

A. Mean flow profiles

Figure 1 schematically shows the flow configuration, a spatially developing mixing layer with its freestream conditions denoted by the subscripts ∞ and $-\infty$, respectively. Two dimensionless parameters are employed to describe the mean flow structure: the velocity ratio, $\Lambda = (U_\infty - U_{-\infty})/(U_\infty + U_{-\infty})$ and the temperature ratio, $S_T = T_\infty/T_{-\infty}$. The former measures the shear strength imposed on the mixing layer and the latter measures the extent of thermophysical property variations. The upper fluid stream is faster than the lower stream, and thus, Λ remains positive. A broad range of temperature and pressure are considered to allow for a systematic study of the fluid flow behavior under different thermodynamic states.

For convenience, a vector \mathbf{q} is defined to represent the primitive variables in Eqs. (1)–(4), $\mathbf{q} = (\rho, u, v, w, T, p)^T$. The flow variable \mathbf{q} is expressed as the sum of the mean and fluctuating quantities

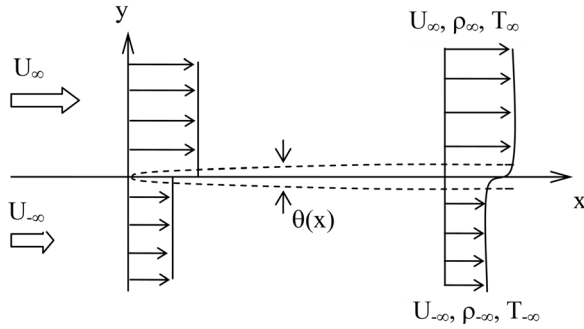


FIG. 1. Schematic of spatially developing mixing layer.

$$\mathbf{q}(x, y, z, t) = \bar{\mathbf{q}}(y, t) + \mathbf{q}'(x, y, z, t). \quad (6)$$

The mean velocity components in the transverse and spanwise directions are neglected, $\bar{v} = \bar{w} = 0$, and $\bar{\mathbf{q}}$ varies only with y and t . The fluctuating component takes the form of a traveling wave with the wave number k and propagating speed c ,

$$\mathbf{q}'(x, y, z, t) = \hat{\mathbf{q}}(y) \exp(ik(x \cos \phi + z \sin \phi - ct)), \quad (7)$$

where $\hat{\mathbf{q}}(y)$ denotes the disturbance amplitude depending only on the transverse coordinate y and ϕ represents the angle between the wave propagation direction and the streamwise direction of the mean flow. When the disturbance aligns with the mean flow direction, ϕ becomes zero and the resultant system becomes a two-dimensional problem. The product of wave number and phase speed gives the angular frequency $\omega = kc$. In general, ω , k , and c are complex numbers with (ω_r, k_r, c_r) in the real part and (ω_i, k_i, c_i) in the imaginary part, respectively. In the spatial stability analysis, the disturbance frequency ω is real ($\omega_i = 0$), and the wave number k and wave speed c are complex. In the temporal stability analysis, the wave number k is real ($k_i = 0$), and the frequency and wave speed are complex.

Following common practice, the above equations are non-dimensionalized using the initial momentum thickness θ , average mean velocity $\bar{U} = (U_\infty + U_{-\infty})/2$, freestream temperature T_∞ , and density ρ_∞ as the characteristic scales. The flow variable vector \mathbf{q} can, thus, be normalized as $\mathbf{q}^* = (\rho^*, u^*, v^*, w^*, T^*, p^*)^T$. The normalized angular frequency $\omega^* = \omega\theta/\bar{U}$ is related to the Strouhal number $St = f\theta/\bar{U}$ as $\omega^* = 2\pi St$. For brevity in notation, the symbol $*$ carried by dimensionless variables is omitted hereafter. The hyperbolic tangent function suggested by Monkewitz and Huerre¹² is used for the mean velocity profile in the present analysis,

$$\bar{u} = 1 + \Lambda \tanh \frac{y}{2}. \quad (8)$$

The normalized mean temperature distribution is similarly expressed by a hyperbolic tangent function,

$$\bar{T} = \frac{S_T + 1}{2} + \frac{S_T - 1}{2} \tanh \frac{y}{2}. \quad (9)$$

The normalized mean pressure is assumed to be unity across the entire space, and the density distribution is obtained accordingly using the selected EOS.

B. Perturbation equations

Substitution of Eqs. (6) and (7) into Eqs. (1)–(4), and then linearization, leads to a set of ordinary differential equations for the perturbation amplitudes,

$$\hat{v}_y = -ik(\bar{u} \cos \phi - c) \frac{\hat{p}}{\rho} - ik \cos \phi \hat{u} - \frac{\bar{\rho}_y}{\rho} \hat{v} - ik \sin \phi \hat{w}, \quad (10)$$

$$ik\bar{\rho}(\bar{u} \cos \phi - c)\hat{u} + \bar{\rho}u_y\hat{v} = -ik \cos \phi \hat{p}, \quad (11)$$

$$\hat{p}_y = -ik\bar{\rho}(\bar{u} \cos \phi - c)\hat{v}, \quad (12)$$

$$\bar{\rho}(\bar{u} \cos \phi - c)\hat{w} = -\sin \phi \hat{p}, \quad (13)$$

$$\hat{T} + \frac{\bar{T}_y}{ik(\bar{u} \cos \phi - c)} \hat{v} = \xi_1 \hat{p}, \quad (14)$$

$$\hat{T} = \xi_2 \hat{p} + \xi_3 \hat{\rho}, \quad (15)$$

where the subscript y denotes the gradient with respect to the vertical coordinate y . The parameters ξ_1 , ξ_2 , and ξ_3 can be determined with the fluid thermodynamic properties as follows:

$$\begin{aligned} \xi_1 &= \frac{\bar{\beta}\bar{T}}{\bar{\rho}C_p}, \\ \xi_2 &= \left[1 - \bar{\rho}R\bar{T} \left(\frac{\partial Z}{\partial p} \right) \bar{T} \right] / \left[\bar{Z}\bar{\rho}R + \bar{\rho}R\bar{T} \left(\frac{\partial Z}{\partial T} \right) \bar{p} \right], \\ \xi_3 &= -\bar{Z}\bar{T} / \left[\bar{Z}\bar{\rho} + \bar{\rho}\bar{T} \left(\frac{\partial Z}{\partial T} \right) \bar{p} \right]. \end{aligned} \quad (16)$$

For ideal gases, Eq. (16) degenerates to

$$\xi_1 = \frac{1}{\bar{\rho}C_p}; \quad \xi_2 = \bar{\rho}R; \quad \xi_3 = -\frac{\bar{T}}{\bar{\rho}}. \quad (17)$$

After multiple manipulations of Eqs. (10)–(15), a second-order ordinary differential equation for the pressure perturbation amplitude is obtained as follows:

$$\hat{p}_{yy} - \left(\frac{2\bar{u}_y \cos \phi}{\bar{u} \cos \phi - c} + \frac{\bar{T}_y}{\xi_3 \bar{\rho}} \right) \hat{p}_y - k^2 \left[1 - (\bar{u} \cos \phi - c)^2 \frac{\xi_1 - \xi_2}{\xi_3} \right] \hat{p} = 0. \quad (18)$$

Equation (18) indicates that the fluctuating field depends strongly on the fluid volumetric properties in terms of the compressibility factor manifested through the coefficients ξ_1 , ξ_2 , and ξ_3 . These quantities vary closely with pressure and temperature, as shown in the generalized compressibility factor chart in Fig. 2, where p_r and T_r are the reduced pressure and temperature. For each isobaric line, there exists a temperature corresponding to the inflection point, across which the compressibility factor changes substantially. The fluid behaves like an ideal gas in the limit of low pressure and high temperature with a compressibility factor of unity.

With the use of the SRK EOS, the parameters ξ_1 , ξ_2 , and ξ_3 can be explicitly written as a function of fluid thermodynamic properties. Equation (18) becomes

$$\hat{p}_{yy} - \left(\frac{2\bar{u}_y \cos \phi}{\bar{u} \cos \phi - c} - \frac{\bar{\beta}\bar{T}_y}{\bar{\rho}} \right) \hat{p}_y - k^2 \left[1 - \frac{(\bar{u} \cos \phi - c)^2}{a^2} \right] \hat{p} = 0. \quad (19)$$

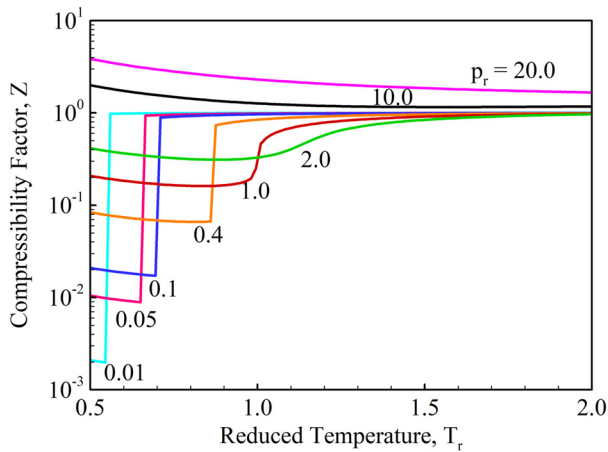


FIG. 2. Compressibility factor of nitrogen as function of temperature and pressure.

In the present study, the mean pressure distribution is uniform. The mean temperature and density gradients are related as $\bar{\beta} \bar{T}_y = -\bar{\rho}_y / \bar{\rho}$. With the introduction of $M \equiv (\bar{u} \cos \phi - c) / \bar{a}$ for simplicity, the dimensionless form of the disturbance equation becomes

$$\hat{p}_{yy} - \left(\frac{2\bar{u}_y \cos \phi}{\bar{u} \cos \phi - c} + \frac{\bar{\rho}_y}{\bar{\rho}} \right) \hat{p}_y - k^2(1 - M^2)\hat{p} = 0. \quad (20)$$

This equation is valid for any fluid mixing layer over the entire range of thermodynamic states, without the inclusion of the diffusion and surface-tension effects. Care must be exercised, however, when applying this equation to problems involving different thermodynamic phases.

Equation (20) appears to be identical to that for ideal gases with mean density variation employed by Shin and Ferziger.¹⁵ As mentioned previously, because of thermodynamic nonideality and property anomaly, the stability characteristics of a real fluid may exhibit features distinct from their ideal gas counterparts. For example, the speed of sound in a real fluid depends on both temperature and pressure but in an ideal gas only on temperature. Figure 3 shows the variation of the speed of sound of nitrogen as a function of temperature at different pressures. At subcritical pressure, the speed of sound decreases with increasing temperature in the liquid phase, reaches its minimum at the boiling point, and then increases in the gas phase. The discontinuity occurs at the liquid-to-gas phase transition. Under supercritical pressure, the trend is qualitatively the same, but rather than a discontinuity, there is a smooth transition from liquid-like to gas-like supercritical fluid. In addition, the magnitude of the relative density gradient of a general fluid $\bar{\rho}_y / \bar{\rho}$ may be dramatically different from that of an ideal gas. The relationship between density and temperature gradients along isobaric lines can be rewritten as $\bar{\rho}_y / \bar{\rho} = -(\bar{\mu}_J \bar{C}_p \bar{\rho} + 1) \bar{T}_y / \bar{T}$, where $\bar{\mu}_J$ is the isothermal Joule–Thomson coefficient.

Figure 4 shows the variation of the correction term $(\bar{\mu}_J \bar{C}_p \bar{\rho} + 1)$ for nitrogen along several isobaric lines. For a real fluid mixing layer, the magnitude of the correction term deviates significantly from unity, especially near the critical point of the substance. A real fluid EOS is required to capture such deviation. At the ideal gas limit, the

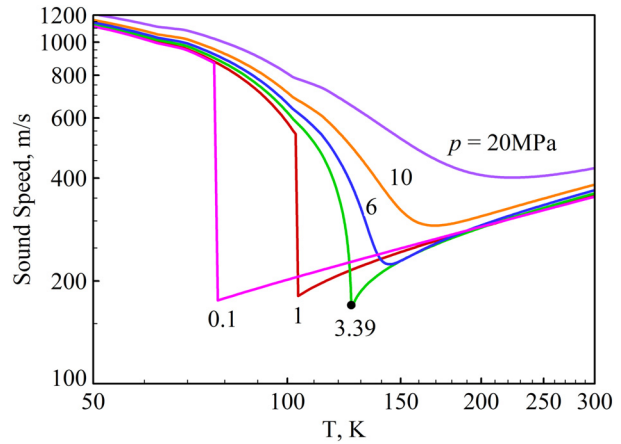


FIG. 3. Sound Speed of nitrogen as a function of temperature at various pressures.

correction term is equal to unity and the disturbance equation for ideal gas mixing layers reduces to

$$\hat{p}_{yy} - \left(\frac{2\bar{u}_y \cos \phi}{\bar{u} \cos \phi - c} - \frac{\bar{T}_y}{\bar{T}} \right) \hat{p}_y - k^2(1 - M^2)\hat{p} = 0. \quad (21)$$

For an incompressible mixing layer, the disturbance equation takes the following form, with the correction term decreasing to zero

$$\hat{p}_{yy} - \left(\frac{2\bar{u}_y \cos \phi}{\bar{u} \cos \phi - c} \right) \hat{p}_y - k^2(1 - M^2)\hat{p} = 0. \quad (22)$$

In the present work, two-dimensional linear stability analysis is conducted and the disturbance governing equation is given by setting $\phi = 0$. That is, the wave propagation direction is identical to the streamwise direction.

C. Boundary conditions

In the far freestream, all the property gradients of the mean flow vanish. Therefore, Eq. (22) for the pressure amplitude is reduced to the following form:

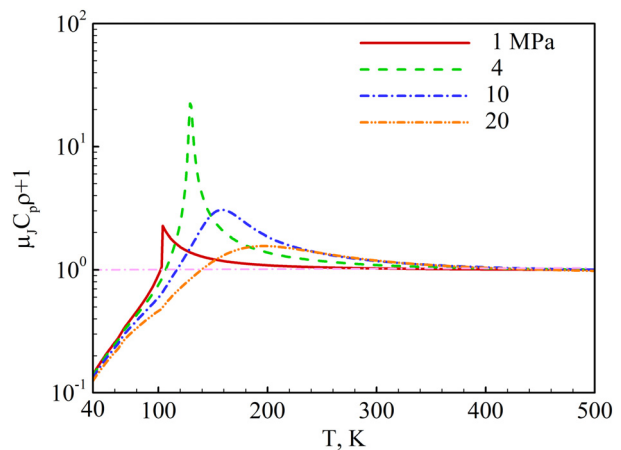


FIG. 4. Variation of correction term with temperature at different pressure.

$$\hat{p}_{yy} - k^2 k_m \hat{p} = 0, \tag{23}$$

where $k_m = 1 - M^2$ represents the fluid compressibility effect. The general solution of Eq. (23) is

$$\hat{p} = A_1 \exp [kk_M y] + A_2 \exp [-kk_M y]. \tag{24}$$

To ensure convergence of the solution, A_1 must vanish at $y = +\infty$ and A_2 at $y = -\infty$. The corresponding boundary conditions become

$$\begin{aligned} \hat{p}|_{y=+\infty} &= A_2 \exp [-kk_M y], \\ \hat{p}_y|_{y=+\infty} &= -A_2 k k_M \exp [-kk_M y], \\ \hat{p}|_{y=-\infty} &= A_1 \exp [kk_M y], \\ \hat{p}_y|_{y=-\infty} &= A_1 k k_M \exp [kk_M y]. \end{aligned} \tag{25}$$

D. Numerical method and validation

The linear stability analysis is essentially an eigenvalue problem with two parameters k and ω in the governing disturbance equation. A shooting technique is applied to solve this problem. A fourth-order Runge–Kutta method is employed to integrate the ordinary differential equation, and the Newton–Raphson method is utilized to search the eigenvalue. Both spatial and temporal stability analyses are conducted. To validate the numerical algorithm, the spatial stability analysis of an incompressible mixing layer is benchmarked against the work of Monkewitz and Huerre.¹² Figure 5 presents variations of the normalized spatial growth rate and wave speed as a function of the Strouhal number at different velocity ratios. Good agreement is achieved for all velocity ratios between the present results and the literature.

III. RESULTS AND DISCUSSION

For spatial stability problems, the objective is to find the most amplified frequency ω_0 that corresponds to the maximum spatial growth rate $-k_i$,

$$\left. \frac{d(-k_i)}{d\omega} \right|_{\omega_0} = 0. \tag{26}$$

For temporal stability problems, the most unstable wavelength $\lambda_0 = 1/k_0$ at which the corresponding maximum growth rate ω_i takes place is determined by

$$\left. \frac{d(\omega_i)}{dk} \right|_{k_0} = 0. \tag{27}$$

The low Mach number assumption is applied to most of the following simulations.

A. Spatial stability of ideal gas mixing layer

In order to investigate the effect of the transverse density distribution on stability characteristics, ideal gas mixing layers are studied with two different mean density profiles $\bar{\rho}_1$ and $\bar{\rho}_2$, given by

$$\bar{\rho}_1 = \left[\frac{S_T + 1}{2} + \frac{S_T - 1}{2} \tanh\left(\frac{y}{2}\right) \right]^{-1}, \tag{28}$$

$$\bar{\rho}_2 = \frac{1/S_T + 1}{2} + \frac{1/S_T - 1}{2} \tanh\left(\frac{y}{2}\right). \tag{29}$$

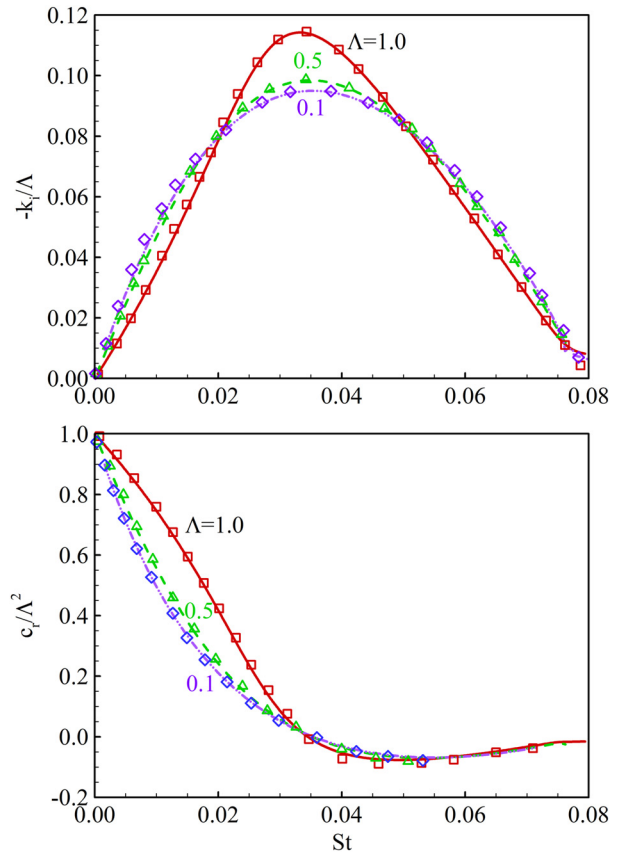


FIG. 5. Normalized spatial growth rate and normalized phase speed as a function of Strouhal number for incompressible flow with various velocity ratios: lines—present results; symbols—results from Monkewitz and Huerre.¹²

The density profile $\bar{\rho}_1$ is obtained by employing the ideal gas EOS for the mixing layer with the temperature distribution defined by Eq. (9), while $\bar{\rho}_2$ is calibrated to have the same freestream density ratio of $S_{\rho,1} = S_{\rho,2} = S_T$, but with slightly different relative density gradients, as shown in Fig. 6.

Figure 7 shows the variation of the spatial growth rate and wave speed with the angular frequency of an ideal gas mixing layer. The velocity ratio varies in the range of 0.25–1.0 and $S_T = 2.5$. The structure of the mean flow has a considerable impact on the stability properties. The growth rate at low frequencies is relatively insensitive to the mean density profiles, whereas it changes significantly at high frequencies. The maximum growth rate increases with increasing velocity ratio, implying enhanced instability downstream. The most unstable frequency, which is associated with the maximum growth rate and wave speed, decreases with increasing velocity ratio.

Figure 8 plots the variation of spatial growth rate with angular frequency for the two density profiles. The freestream temperature ratio varies between 0.2 and 2.5 with a constant velocity ratio of 1.0. With increasing density ratio, the peak spatial growth rate increases and the most unstable frequency monotonically

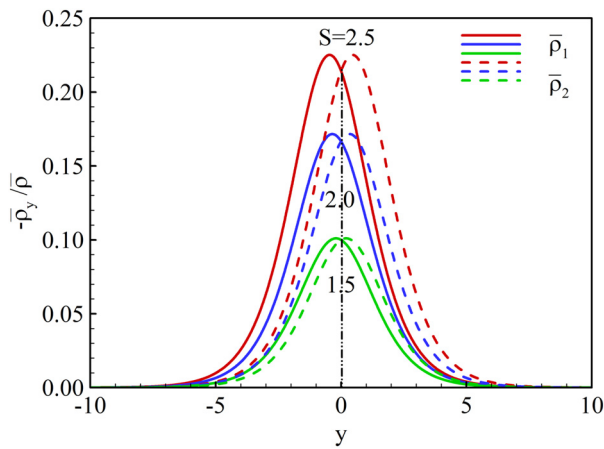


FIG. 6. Relative density variation of density profiles $\bar{\rho}_1$ and $\bar{\rho}_2$.

decreases. A lighter fluid stream with a higher velocity tends to increase the spatial growth rate. The most unstable mode depends strongly on the mean flow profile, for the cases with large density stratification.

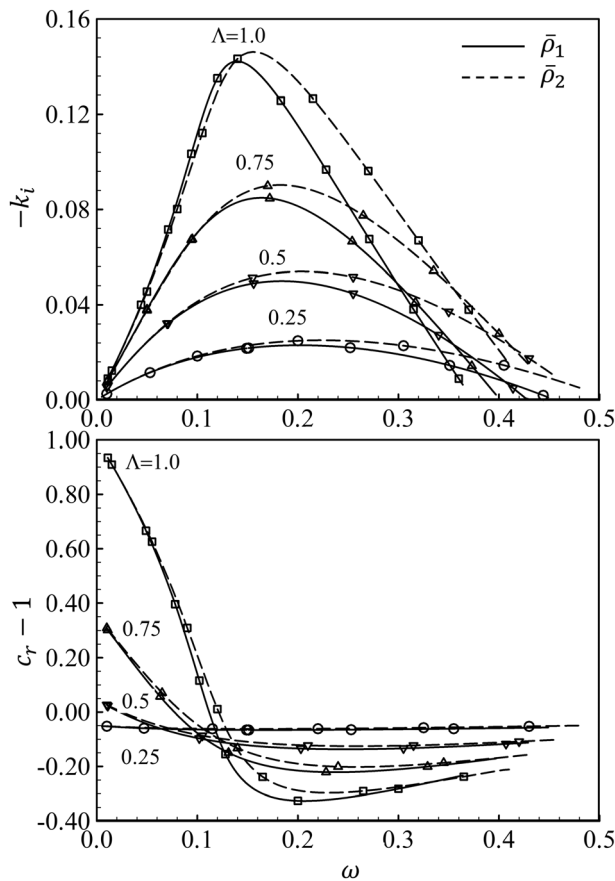


FIG. 7. Variations of spatial growth rate and phase speed with angular frequency: ideal gas mixing layer at various velocity ratios and $S_T = 2.5$.

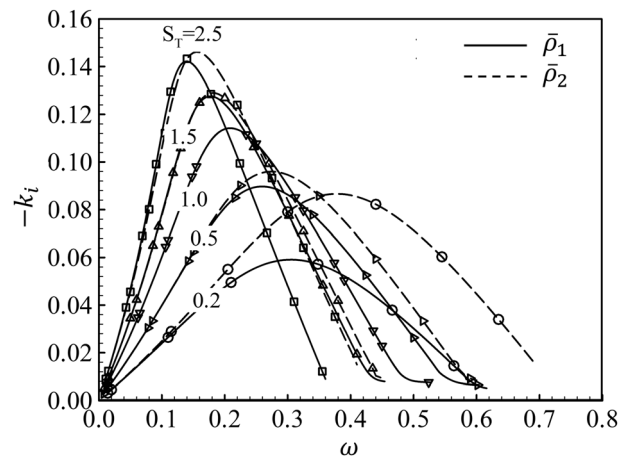


FIG. 8. Variation of spatial growth rate with angular frequency: ideal gas mixing layer at various temperature ratios and $\Lambda = 1.0$.

B. Spatial stability of real fluid mixing layer

Unlike an ideal gas mixing layer, a real fluid mixing layer exhibits strong asymmetry of the mean density profile $\bar{\rho}_y/\bar{\rho}$, especially near the critical point, so the stability properties of the real fluid mixing layer are quite distinct from their ideal gas counterparts. The spatial stability of variable-density mixing layers of nitrogen is studied by taking into account real fluid effects at supercritical pressures. For reference, the critical temperature and pressure of nitrogen are 126 K and 3.4 MPa, respectively. The ambient mean pressure varies from 4 to 10 MPa. The density distributions are obtained by solving the SRK EOS with pre-specified temperature distributions in Eq. (9), denoted as $\bar{\rho}_{SRK}$. The density ratio S_ρ can be determined correspondingly, in particular, $S_\rho = 5.6$ at the pressure of 10 MPa and $S_\rho = 11.6$ at the pressure of 4 MPa. For comparison, ideal gas mixing layers with density distributions $\bar{\rho}_1$ and $\bar{\rho}_2$ with the same freestream density ratio are also considered. This enables us to explore the net effect of density distribution on the characteristics of flow instability.

Figure 9 shows the normalized spatial growth rates as a function of the Strouhal number and the transverse distributions of the relative density gradient $(\bar{\rho}_y/\bar{\rho})$ and momentum flux gradient $((\bar{\rho}u^2)_y/\bar{\rho}u^2)$. Three different density distributions are considered at 4 and 10 MPa. The temperature and velocity ratios are fixed at 2.5 and 0.5, respectively. At 4 MPa, the density distribution $\bar{\rho}_{SRK}$ leads to a substantially lower maximum spatial growth rate, and the most unstable Strouhal number becomes smaller than with ideal gas density profiles $\bar{\rho}_1$ and $\bar{\rho}_2$. This pressure condition is close to the critical point (3.4 MPa) of nitrogen and thereby induces a strong real fluid behavior. The resultant density profile imposes a crucial influence on the stability characteristics of the mixing layer. At 10 MPa, on the other hand, the results associated with the density distribution $\bar{\rho}_1$ show good agreement with those with $\bar{\rho}_{SRK}$, implying that the ideal gas EOS is sufficient for the evaluation of spatial stability at such pressure. The density distribution $\bar{\rho}_2$ leads to overestimation of the maximum growth rate and Strouhal number at both pressure levels. The transverse distributions of the relative density and momentum-flux gradients associated with the density profiles $\bar{\rho}_1$ and $\bar{\rho}_2$ present large deviations from those of $\bar{\rho}_{SRK}$ for both pressure conditions. The real fluid EOS is, thus, critical to the

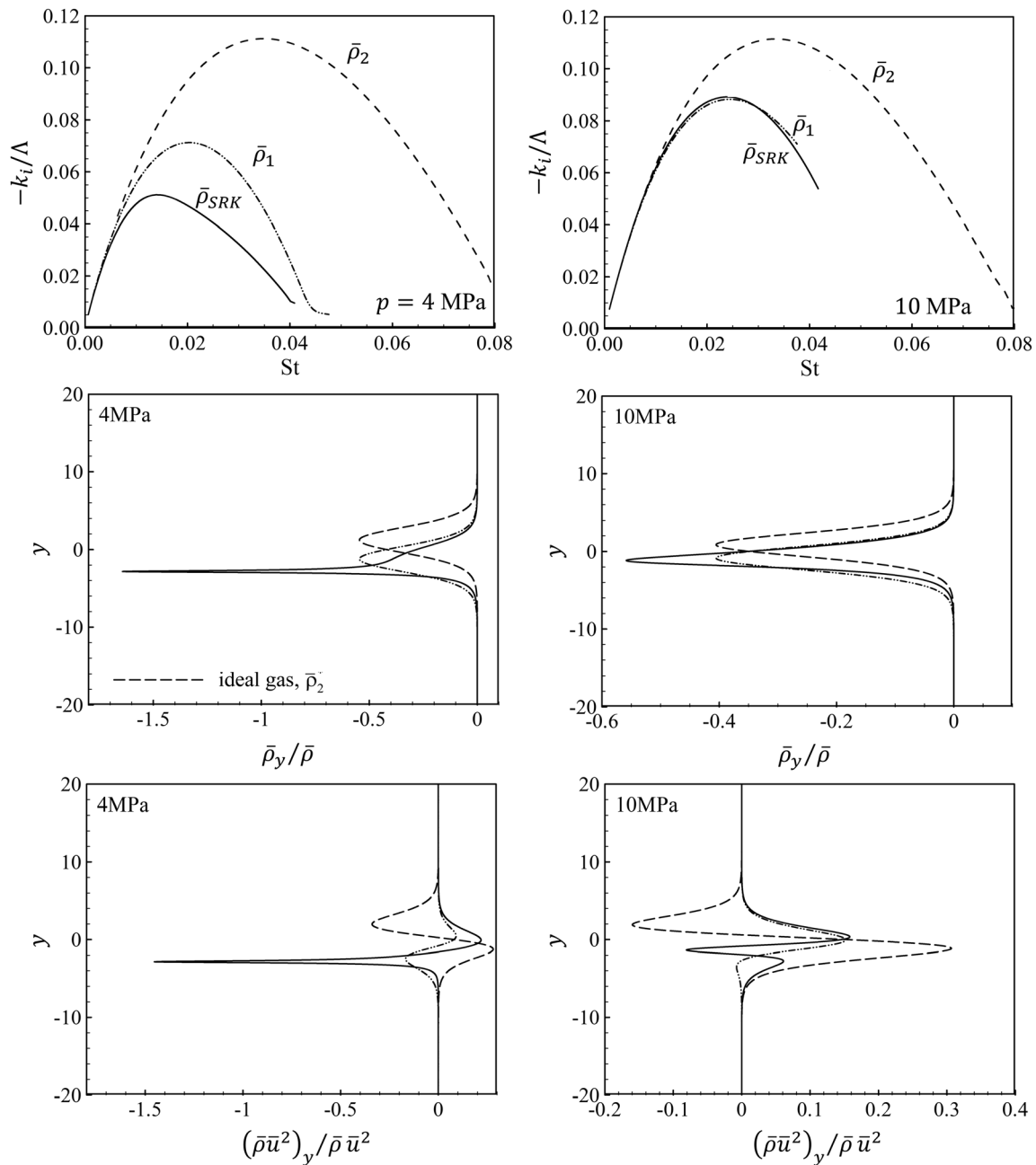


FIG. 9. Variation of normalized spatial growth rate as a function of Strouhal number (upper) and transverse distributions of relative density (middle) and momentum flux (lower) gradients, for three different density distributions, at 4 and 10 MPa.

prediction of flow properties and instability behaviors at supercritical pressures. In the following simulations of this subsection, only $\bar{\rho}_1$ is used for comparison since $\bar{\rho}_2$ results in large errors.

In order to obtain deeper insight into the effects of freestream density ratio and density distribution near the critical point, the spatial stability characteristics at 4 MPa and a velocity ratio of 0.5 were obtained, as shown in Fig. 10. The temperature ratio S_T varies from

1.5 to 4.0 with three different sets of freestream temperatures $(T_{-\infty}, T_{\infty})$: (120, 180), (120, 300), (125, 500) K, as shown in Fig. 11. The corresponding density ratio S_ρ determined by the SRK EOS falls in the range of 6.1–16.7. For real fluids, the lower density ratio ($S_\rho = 6.1$) tends to destabilize the mixing layer with a higher maximum growth rate, while a higher density ratio ($S_\rho = 16.7$) induces a slightly higher most unstable frequency. The ideal gas approach

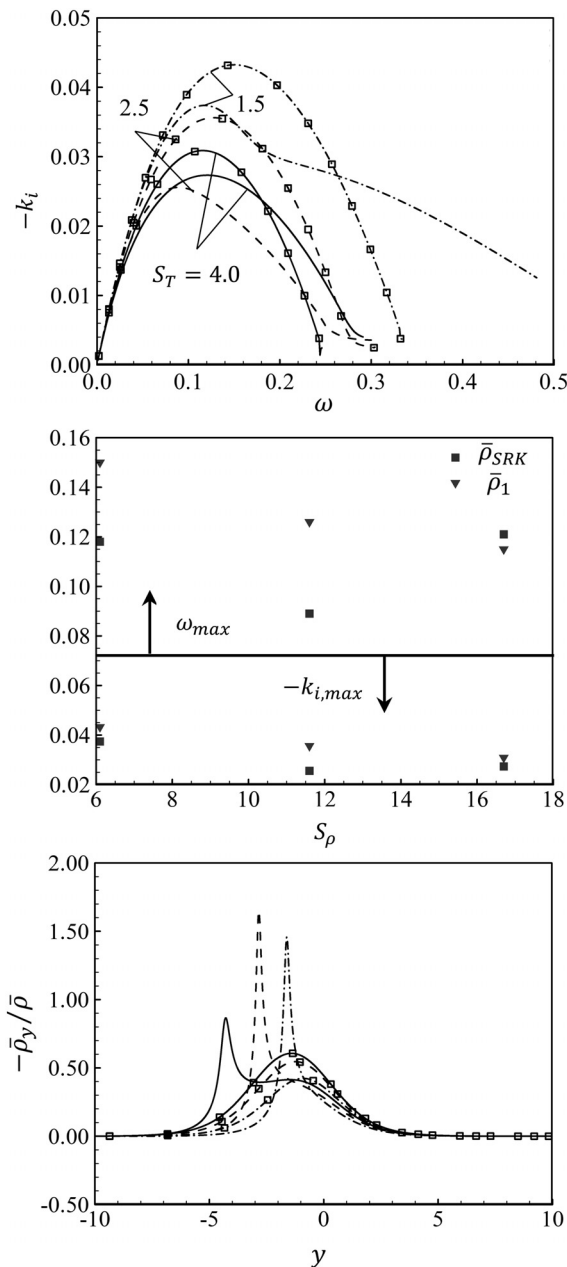


FIG. 10. Variation of spatial growth rate as a function of angular frequency (top), maximum spatial growth rate and most unstable frequency (middle), and transverse distributions of relative density gradient (bottom) at different temperature ratios at 4 MPa (lines: $\bar{\rho}_{SRK}$; symbols: $\bar{\rho}_1$).

consistently fails to predict the maximum growth rate and associated frequency information at different density ratios. The underlying reason may be the under-estimation of the density gradient by the ideal gas approach near the inflection point, where the gradient of density with respect to temperature is steepest and is well predicted by the SRK EOS, as shown in the $\rho - T$ diagram in Fig. 11. The mean density gradient $\bar{\rho}_y$ can be related to $\partial\rho/\partial T$ (ρ_T) using the chain rule

$$\bar{\rho}_y = \bar{\rho}_T \bar{T}_y. \tag{30}$$

The inflection point at 4 MPa is found to be 129 K. The increase of the density ratio moves the inflection point further away from the centerline, and this trend is not obvious for ideal gas. The density ratio increases substantially when the inflection point is located in the mixing layer. The density gradients determined by Eq. (30) are quite different for different temperature ranges and their distributions. The presence of the inflection point in the mixing layer dictates the importance of real fluid effects in the spatial stability analysis.

To further illustrate the effect of the inflection point, Fig. 12 shows the stability characteristics of nitrogen mixing layers for four different temperature ranges: (333–500), (200–500), (131–500), and (125–500) K. The temperature ratio increases from 1.5 to 4.0. Among these cases, only one ($S_T = 4.0$) covers the inflection point. The case with the largest temperature ratio has the smallest most unstable frequency and the smallest growth rate because of its largest relative density gradient. For cases in the absence of the inflection point, the ideal gas approach gives reasonable agreement with the real fluid counterpart, especially when the lower temperature limit moves away from the inflection point.

All of the above analyses are based on the low Mach number assumption, which generally is a good approximation for Mach numbers below 0.3. However, the Mach number effect needs to be included when the mean flow velocity is comparable to the speed of sound. Figure 13 shows the effect of Mach number on the stability characteristics as the freestream velocity increases from 1 to 500 m/s at 4 MPa. The stability of the mixing layer is considerably improved, as manifested by the decreasing of the maximum growth rate and the most unstable frequency. The maximum growth rate is reduced by more than 50% when the mean velocity increases from 100 to 300 m/s.

C. Spatial stability of two-dimensional jets

In this subsection, the spatial stability analysis of two-dimensional jets is studied. The mean flow velocity and temperature profiles have functional forms similar to those described by Yu and Monkewitz,¹³

$$\begin{aligned} \bar{u}(y) &= 1 - \Lambda_c + 2\Lambda_c F(y), \\ F(y) &= [1 + \sinh^{2N}(y \operatorname{arcsinh} 1)]^{-1}, \\ \bar{T}(y) &= 1 + (S_c^{-1} - 1)F(y), \end{aligned} \tag{31}$$

where N is the shape factor; Λ_c is the velocity ratio, defined as $\Lambda_c \equiv (\bar{U}_c - \bar{U}_\infty)/(\bar{U}_c + \bar{U}_\infty)$; and S_c is the temperature ratio, $S_c \equiv \bar{T}_\infty/\bar{T}_c$. \bar{U}_c and \bar{T}_c are the velocity and temperature, respectively, at the centerline. The shape factor N controls the velocity gradient and momentum thickness of the mixing layer. Figure 14 presents the velocity profile and momentum thickness as a function of the shape factor. A larger shape factor leads to a stronger velocity gradient and thinner momentum thickness.

As in the mixing layer analyses above, two different density profiles, $\bar{\rho}_1$ and $\bar{\rho}_{SRK}$, are introduced through a prescribed temperature distribution in Eq. (31), following the ideal gas and real fluid approaches, and a third-density profile $\bar{\rho}_2$ with the same density ratio as $\bar{\rho}_1$ is also included. The disturbance equation and the boundary

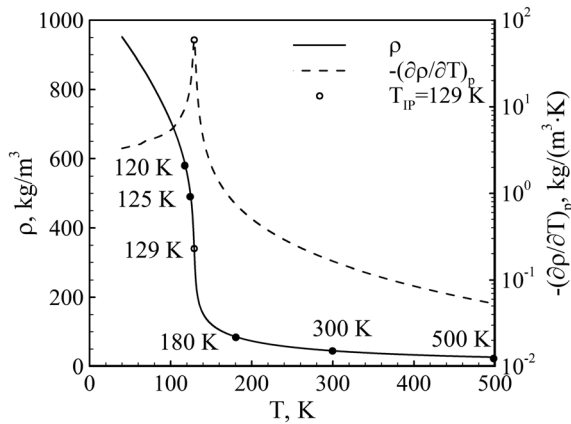


FIG. 11. Distribution of density and density gradient with respect to temperature at 4 MPa (IP: inflection point).

conditions are the same as those for the mixing layer, see Eq. (25). The centerline boundary conditions are given by assuming flow symmetry

$$\hat{p}|_{y=0} = 1, \quad \frac{d\hat{p}}{dy}|_{y=0} = 0. \quad (32)$$

Figure 15 shows the variation of the spatial growth rate with the angular frequency at different velocity ratios for density profiles $\bar{\rho}_1$ and $\bar{\rho}_2$. The temperature ratio is fixed at $S_T = 2.5$. The maximum growth rate and the most unstable frequency increase with increasing velocity ratio. The most unstable frequency and growth rate of the jet with $\bar{\rho}_2$ are larger than those with $\bar{\rho}_1$. These phenomena again demonstrate the importance of the details of the density distribution in the study of instability characteristics. Figure 16 shows the variation of the maximum spatial growth rate and the most unstable angular frequency at different density ratios using both real fluid and ideal gas density profiles. The velocity ratio is fixed at 1.0. The results associated with the real fluid density profile differ considerably from their ideal

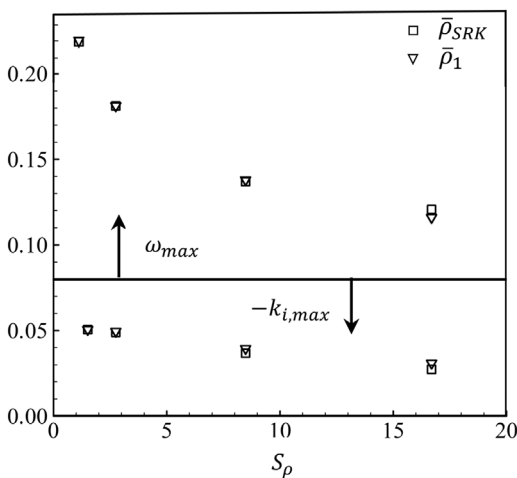


FIG. 12. Maximum spatial growth rate and most unstable frequency at different density ratios at 4 MPa.

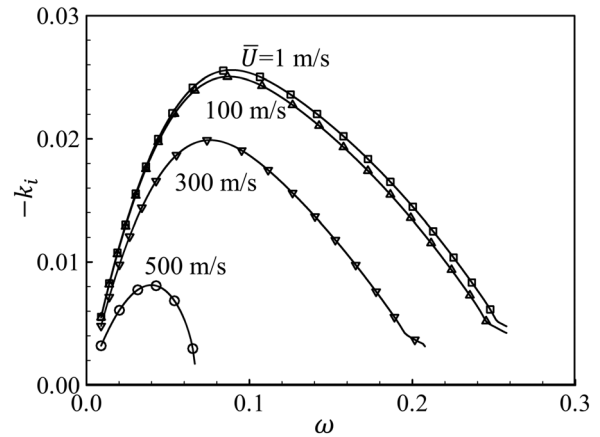


FIG. 13. Variation of spatial growth rate with angular frequency at different mean flow velocities ($p = 4$ MPa, $T_{-\infty} = 120$ K, $T_{\infty} = 300$ K).

gas counterparts. With increasing density ratio, the frequency decreases in the real fluid case but increases in the ideal gas case. Although the maximum growth rate decreases with the density ratio in both cases, the decreasing rate is larger in the ideal gas approach.

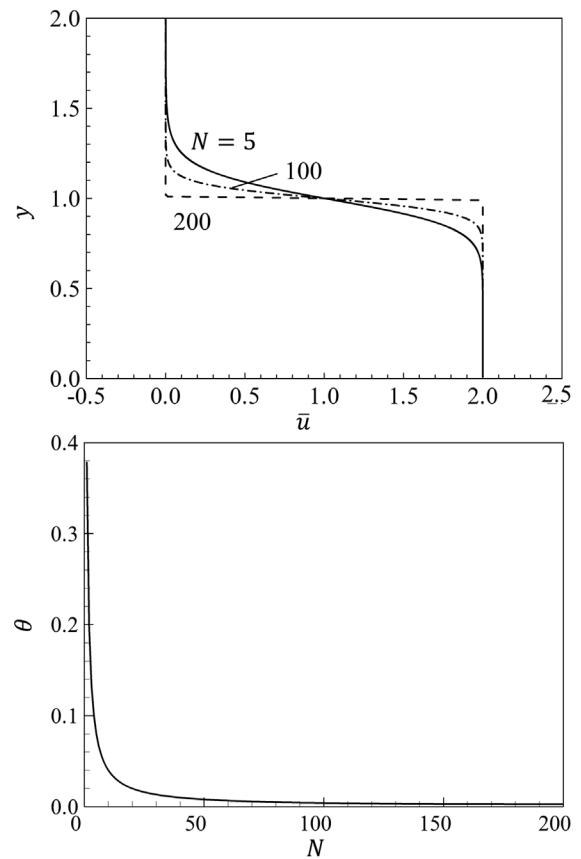


FIG. 14. Dimensionless mean velocity and momentum thickness as function of shape factor N .

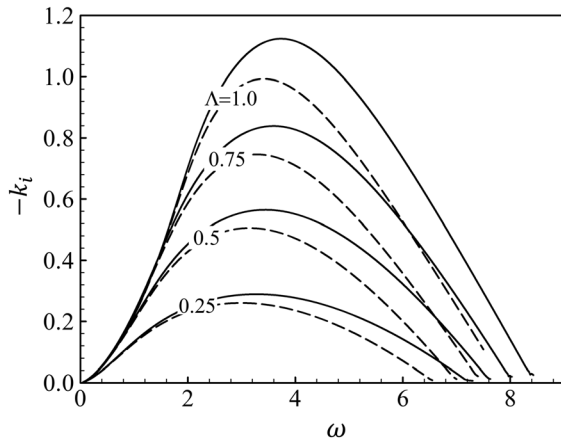


FIG. 15. Variation of spatial growth rate with angular frequency at different velocity ratios and constant temperature ratio of 2.5 (dashed lines: $\bar{\rho}_1$; solid lines: $\bar{\rho}_2$).

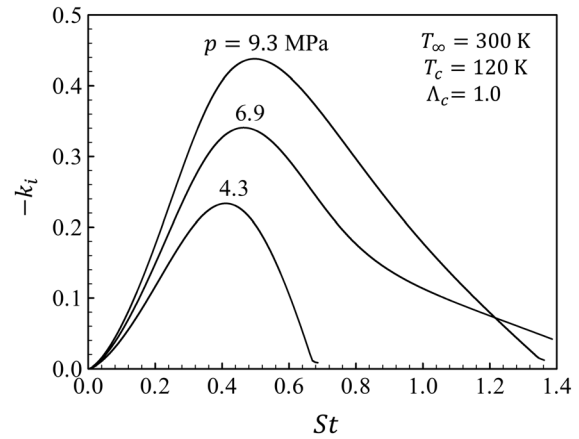


FIG. 17. Variation of spatial growth rate with Strouhal number at different supercritical pressures with $\Lambda_c = 1.0$, $T_c = 120$ K, and $T_\infty = 300$ K.

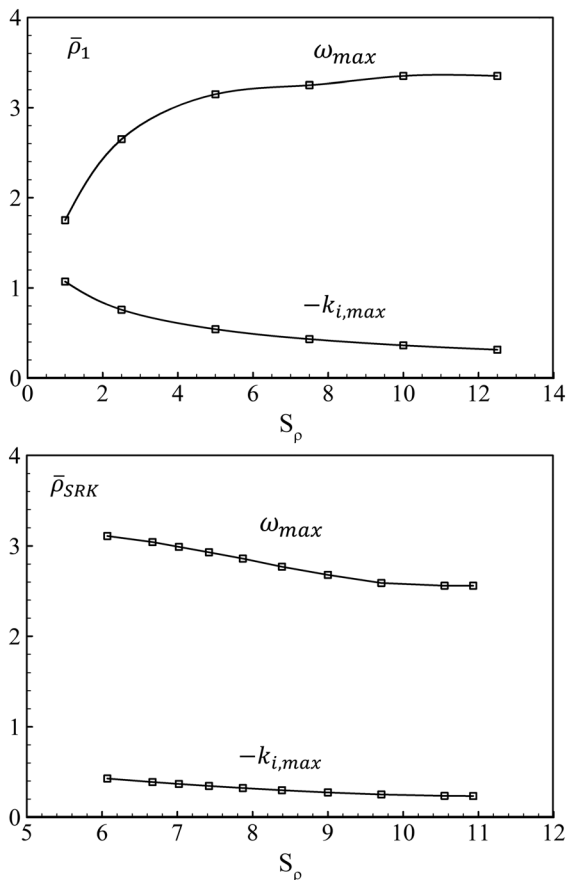


FIG. 16. Variation of maximum spatial growth rate and most unstable angular frequency at different density ratios with $\Lambda_c = 1.0$.

Figure 17 shows the spatial growth rate as a function of the Strouhal number at different supercritical pressures. The maximum growth rate and the most unstable Strouhal number increase with increasing pressure. This result is consistent with the dominant frequency predicted by high-fidelity numerical simulations of cryogenic nitrogen injection and mixing,²⁴ and the dominant frequency agrees well with the most amplified frequency of the shear layer instability. Increasing pressure tends to promote unstable flow motion and enhance mixing. The real fluid EOS is critical for accurate prediction of the density distribution and enabling the capture of spatial instability during the initial development of the jet injection and mixing processes.

D. Temporal stability of mixing layer

In temporal stability analysis, wave number is real and frequency is complex. Figure 18 shows the variation of the normalized temporal growth rate (ω_i/Λ) with the wave number at 4 MPa for density profiles described previously. The velocity ratio ranges from 0.25 to 1.0, and the temperature ratio remains constant at 2.5. The normalized growth rates for a given density profile merge into a single curve, which implies that the temporal growth rate is directly proportional to the velocity ratio regardless of the density distribution. This may be attributed to the intrinsic relationship between the imaginary part of frequency and the velocity ratio embedded in the coefficient of the first-order gradient of the pressure disturbance magnitude (\hat{p}_y) in Eq. (20). The stability results predicted from the ideal gas density profiles overestimate both the maximum temporal growth rate and the associated most unstable wave number, compared to those predicted from real fluid density profile based on the SRK EOS.

The effect of the details of density distribution on the development of temporal instability is further explored by varying the free-stream temperature ratio. Figure 19 shows temporal stability results for mixing layers at a pressure of 4 MPa. The temperature and density ratios are the same as those in Fig. 10. The results associated with the real fluid density profile ($\bar{\rho}_{SRK}$) show that the most unstable wave number for the density ratio of 16.7 is slightly larger than that for the other two ratios, and the maximum normalized growth rate is the

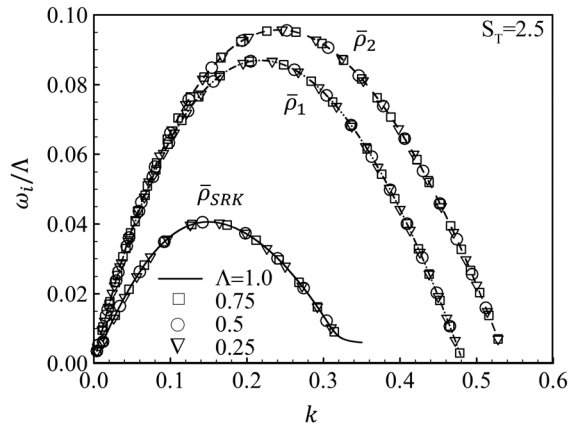


FIG. 18. Variation of normalized temporal growth rate with wave number for various supercritical pressures and density profiles ($p = 4$ MPa, $T_{-\infty} = 120$ K, and $T_{\infty} = 300$ K).

highest at a density ratio of 6.1. The results associated with the ideal gas density profile ($\bar{\rho}_1$) indicate that both the maximum normalized temporal growth rate and the most unstable wavenumber decrease with increasing density ratio. The detailed density distribution has a crucial impact on temporal stability properties at supercritical pressure. The discrepancy between the ideal gas and real fluid density profiles decreases as the temperature/density ratio increases.

Figure 20 shows the variation of the normalized temporal growth rate with wave number at two different supercritical pressures using the real fluid and ideal gas density profiles. The most unstable wavelength calculated with $\bar{\rho}_{SRK}$ is larger than that with $\bar{\rho}_1$, while the maximum temporal growth rate shows an opposite trend. The difference of instability properties between the two density profiles becomes smaller from 4 to 10 MPa, mainly due to the fact that the inflection point of the latter is farther from the critical point than the former. A similar conclusion was drawn earlier for the spatial stability analysis. This emphasizes the crucial influence of the inflection point and resultant density stratification on the linear stability analysis at supercritical pressure.

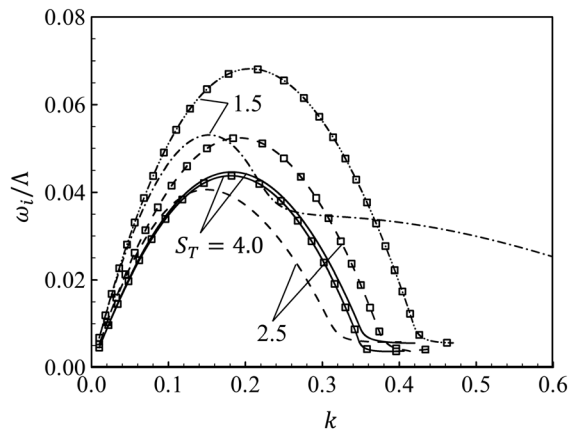


FIG. 19. Variation of normalized temporal growth rate with wave number for various temperature ratios (lines: $\bar{\rho}_{SRK}$; symbolic lines: $\bar{\rho}_1$).

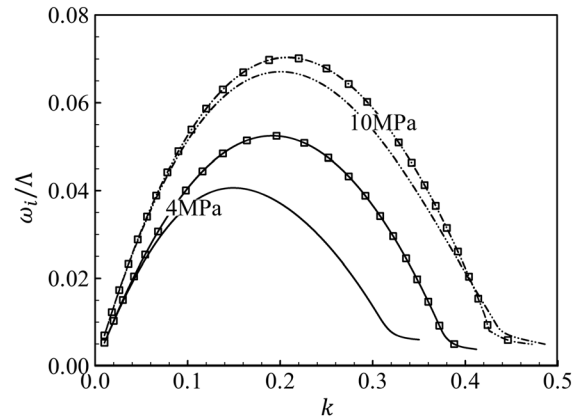


FIG. 20. Variation of normalized temporal growth rate with wave number at two supercritical pressures (lines: $\bar{\rho}_{SRK}$; symbolic lines: $\bar{\rho}_1$).

IV. CONCLUSION

Linear stability of real fluid mixing layers has been comprehensively investigated at supercritical conditions, with particular attention to the effect of density stratification induced by the velocity and temperature differences across the mixing layer. A generalized inviscid disturbance equation for real fluid mixing layers was derived, covering the range of thermodynamic states of fluids. Both spatial and temporal stability analyses were performed using hyperbolic tangent mean flow profiles. The detailed density distribution in the mixing layer was found to play a dominant role in determining the stability characteristics of the fluctuating field.

The density profiles obtained using the ideal gas and real fluid approaches were systematically examined. When an inflection of the density distribution exists in the mixing layer, the induced strong density stratification tends to stabilize the mixing layer. The resultant maximum spatial growth rate and the most unstable frequency determined from the real fluid approach are substantially lower than their ideal gas counterparts and do not show monotonic trends with density and temperature ratios. Outside of the inflection point, however, the maximum spatial growth rate and the most unstable frequency increase with increasing pressure and decreasing ratios of density and temperature. The real fluid effect on mixing-layer stability is smaller when the density profile does not contain an inflection in the mixing layer or when the pressure is far from the critical value. In terms of temporal stability, the normalized temporal growth rates merge into a single curve at a given temperature ratio and pressure. The details of the density distribution also play a key role in determining the temporal behaviors of mixing-layer stability.

AUTHOR DECLARATIONS

Conflict of Interest

The authors have no conflicts to disclose.

Author Contributions

Xingjian Wang: Investigation (equal), Methodology (equal), Visualization (equal), Writing – original draft (equal), and Writing – review and editing (equal). **Tao Liu:** Conceptualization (equal),

Methodology (equal), Visualization (equal), and Writing – original draft (supporting). **Dongjun Ma:** Methodology (supporting), Supervision (supporting), and Writing – review and editing (supporting). **Vigor Yang:** Conceptualization (equal), Methodology (equal), Supervision (equal), and Writing – review and editing (equal).

DATA AVAILABILITY

The data that support the findings of this study are available from the corresponding authors upon reasonable request.

REFERENCES

- ¹R. W. Metcalfe, S. A. Orszag, M. E. Brachet, S. Menon, and J. J. Riley, “Secondary instability of a temporally growing mixing layer,” *J. Fluid Mech.* **184**, 207–243 (1987).
- ²N. Zong and V. Yang, “Cryogenic fluid jets and mixing layers in transcritical and supercritical environments,” *Combust. Sci. Technol.* **178**(1–3), 193–227 (2006).
- ³X. Fang, C. Shen, M. Sun, and Z. Hu, “Effects of oblique shock waves on turbulent structures and statistics of supersonic mixing layers,” *Phys. Fluids* **30**(11), 116101 (2018).
- ⁴D. Zhang, J. Tan, and X. Yao, “Direct numerical simulation of spatially developing highly compressible mixing layer: Structural evolution and turbulent statistics,” *Phys. Fluids* **31**(3), 036102 (2019).
- ⁵Q. Dai, T. Jin, K. Luo, and J. Fan, “Direct numerical simulation of a three-dimensional spatially evolving compressible mixing layer laden with particles. I. Turbulent structures and asymmetric properties,” *Phys. Fluids* **31**(8), 083303 (2019).
- ⁶B. W. Davis, J. Poblador-Ibanez, and W. A. Sirignano, “Two-phase developing laminar mixing layer at supercritical pressures,” *Int. J. Heat Mass Transfer* **167**, 120687 (2021).
- ⁷T. Liu, X. Wang, and V. Yang, “Flow dynamics of shear-coaxial cryogenic nitrogen jets under supercritical conditions with and without acoustic excitations,” *Phys. Fluids* **33**(7), 076111 (2021).
- ⁸U. Unnikrishnan, H. Huo, X. Wang, and V. Yang, “Subgrid scale modeling considerations for large eddy simulation of supercritical turbulent mixing and combustion,” *Phys. Fluids* **33**(7), 075112 (2021).
- ⁹J. Tan, D. Zhang, and L. Lv, “A review on enhanced mixing methods in supersonic mixing layer flows,” *Acta Astronaut.* **152**, 310–324 (2018).
- ¹⁰C.-M. Ho and P. Huerre, “Perturbed free shear layers,” *Annu. Rev. Fluid Mech.* **16**(1), 365–422 (1984).
- ¹¹P. Huerre and P. A. Monkewitz, “Local and global instabilities in spatially developing flows,” *Annu. Rev. Fluid Mech.* **22**(1), 473–537 (1990).
- ¹²P. A. Monkewitz and P. Huerre, “Influence of the velocity ratio on the spatial instability of mixing layers,” *Phys. Fluids* **25**(7), 1137–1143 (1982).
- ¹³M. H. Yu and P. A. Monkewitz, “The effect of nonuniform density on the absolute instability of two-dimensional inertial jets and wakes,” *Phys. Fluids A: Fluid Dyn.* **2**(7), 1175–1181 (1990).
- ¹⁴N. Sandham and W. Reynolds, “Compressible mixing layer-linear theory and direct simulation,” *AIAA J.* **28**(4), 618–624 (1990).
- ¹⁵D. Shin and J. H. Ferziger, “Linear stability of the reacting mixing layer,” *AIAA J.* **29**(10), 1634–1642 (1991).
- ¹⁶F. Kozusko, D. Lasseigne, C. Grosch, and T. Jackson, “The stability of compressible mixing layers in binary gases,” *Phys. Fluids* **8**(7), 1954–1963 (1996).
- ¹⁷M. Day, W. Reynolds, and N. Mansour, “The structure of the compressible reacting mixing layer: Insights from linear stability analysis,” *Phys. Fluids* **10**(4), 993–1007 (1998).
- ¹⁸C. A. Kennedy and J. H. Chen, “Mean flow effects on the linear stability of compressible planar jets,” *Phys. Fluids* **10**(3), 615–626 (1998).
- ¹⁹I. Fedoun and N. Lardjane, “Temporal linear stability analysis of three-dimensional compressible binary shear layers,” *AIAA J.* **43**(1), 111–123 (2005).
- ²⁰R. Rangel and W. Sirignano, “The linear and nonlinear shear instability of a fluid sheet,” *Phys. Fluids A: Fluid Dyn.* **3**(10), 2392–2400 (1991).
- ²¹V. Yang, “Modeling of supercritical vaporization, mixing, and combustion processes in liquid-fueled propulsion systems,” *Proc. Combust. Inst.* **28**(1), 925–942 (2000).
- ²²X. Wang, H. Huo, U. Unnikrishnan, and V. Yang, “A systematic approach to high-fidelity modeling and efficient simulation of supercritical fluid mixing and combustion,” *Combust. Flame* **195**, 203–215 (2018).
- ²³J. Bellan, “Supercritical (and subcritical) fluid behavior and modeling: Drops, streams, shear and mixing layers, jets and sprays,” *Prog. Energy Combust. Sci.* **26**(4–6), 329–366 (2000).
- ²⁴N. Zong, H. Meng, S.-Y. Hsieh, and V. Yang, “A numerical study of cryogenic fluid injection and mixing under supercritical conditions,” *Phys. Fluids* **16**(12), 4248–4261 (2004).
- ²⁵A. Roy and C. Segal, “Experimental study of fluid jet mixing at supercritical conditions,” *J. Propul. Power* **26**(6), 1205–1211 (2010).
- ²⁶N. Okong’o and J. Bellan, “Real-gas effects on mean flow and temporal stability of binary-species mixing layers,” *AIAA J.* **41**(12), 2429–2443 (2003).
- ²⁷P. Yecko, S. Zaleski, and J.-M. Fullana, “Viscous modes in two-phase mixing layers,” *Phys. Fluids* **14**(12), 4115–4122 (2002).
- ²⁸T. Boeck and S. Zaleski, “Viscous versus inviscid instability of two-phase mixing layers with continuous velocity profile,” *Phys. Fluids* **17**(3), 032106 (2005).
- ²⁹R. Govindarajan and K. C. Sahu, “Instabilities in viscosity-stratified flow,” *Annu. Rev. Fluid Mech.* **46**(1), 331–353 (2014).
- ³⁰A. Roy and C. Segal, “Linear stability analysis of a sub-to-supercritical jet,” *Phys. Fluids* **24**(3), 034104 (2012).
- ³¹Q. Fu and L. Yang, “Temporal instability of a transcritical shear layer,” *J. Propul. Power* **32**(5), 1292–1297 (2016).
- ³²Q. Fu, Y. Zhang, C. Mo, and L. Yang, “Instability of a shear layer between multicomponent fluids at supercritical pressure,” *AIP Adv.* **8**(4), 045201 (2018).
- ³³G. Soave, “Equilibrium constants from a modified Redlich-Kwong equation of state,” *Chem. Eng. Sci.* **27**(6), 1197–1203 (1972).